Meccanica (2025) 60:2107–2124
https://doi.org/10.1007/s11012-025-01977-5

RESEARCH

Image-based structural kinematic limit analysis for historical masonry structures

Yahroun Fei Long Hermans · Karim Ehab Moustafa Kamel · Olivier Debeir · Gabriele Milani · Thierry Jacques Massart

Received: 14 September 2024 / Accepted: 24 March 2025 / Published online: 30 April 2025

Abstract Evaluating the state of historical masonry structures, particularly those built with irregular masonry, presents challenges in determining their load-bearing capacity. Most current approaches use macroscopic numerical models that treat the material as a homogeneous continuum, where defining an appropriate constitutive law is essential. To this end, homogenization has proven useful in bridging the gap between meso and macro-scales, yet using homogenized macromodels may prevent to capture specific failure modes. Alternatively, mesoscopic methodologies represent stacking modes explicitly. However, full structural analysis at this scale has mainly been applied to regular masonry due to the complexities of explicitly representing the geometry of the irregular stones. The present contribution aims to propose a method that leverages image acquisition techniques, such as orthophotos, to address these challenges. Mortar joints are lumped onto zero-thickness interfaces, determined through a distance field-based morphing procedure and medial axis principles. The load-bearing capacity is assessed using a Kinematic Limit Analysis problem, formulated and solved as a linear programming problem. A Mohr-Coulomb frictional behavior, modified with a tensile cut-off and a linearized compression cap, is assigned to the mortar joints. The blocks are considered infinitely rigid and strong. It is shown that the proposed methodology can efficiently model structures of large sizes, by illustrating its use on two 2D problems.

Keywords Irregular masonry · Limit analysis · Distance fields · Image-based modelling

Karim Ehab Moustafa Kamel, Olivier Debeir, Gabriele Milani and Thierry Jacques Massart these authors contributed equally to this work.

Y. F. L. Hermans · K. Ehab Moustafa Kamel · T. J. Massart (✉)
Building, Architecture and Town Planning Department (BATir), Université libre de Bruxelles, Avenue CP 194/02 F.D. Roosevelt 50, 1050 Brussels, Brussels, Belgium
e-mail: thierry.j.massart@ulb.be

Y. F. L. Hermans
e-mail: yahroun.fei.hermans@ulb.be

K. Ehab Moustafa Kamel
e-mail: karim.ehab.moustafa.kamel@ulb.be

Y. F. L. Hermans · O. Debeir
Laboratory of Image Synthesis and Analysis, Université libre de Bruxelles, Avenue CP 165/57 F.D. Roosevelt 50, 1050 Brussels, Brussels, Belgium
e-mail: olivier.debeir@ulb.be

Y. F. L. Hermans · G. Milani
Department of Architecture, Built Environment and Construction Engineering (ABC), Technical University of Milan, Piazza Leonardo da Vinci 32, 20133 Milan, Lombardy, Italy
e-mail: gabriele.milani@polimi.it

1 Introduction

Throughout history, numerous architectural and engineering structures have been constructed using masonry. Many of these historical structures are fashioned from either irregular or rubble stone masonry. Despite the prevalent use of this construction method [1], accurately assessing the load-bearing capacity of historical masonry structures remains challenging.

The contributions investigating notable historical masonry structures are numerous. Without exhaustivity, contributions addressing this topic at the scale of structures include contributions by [2] who analyzed structural damage in a church in the Poblet Monastery, by [3] who assessed damage in masonry palaces using nonlinear dynamic analyses, or by [4] in which the Mallorca Cathedral was studied in terms of the construction process and long term effects by means of continuum FE models. The monastery of Jeronimos in Lisbon was the topic of failure analyses in [5], while earthquake-induced damage in the Ica Cathedral in Peru was studied in [6], and the response to seismic events of churches from Emilia-Romagna was investigated in [7]. These contributions and others have shown that computational analysis tools in all their diversity can bring insight in the structural behaviour of masonry historical structures. Detailed discussions on the different methods and strategies for this purpose with respect to available data and intended level of details were discussed in [8], and the relevance of computational modelling for masonry structures was addressed in the review paper [9].

The contributions on the computational methodologies for historical masonry structures may be classified according to different criteria.

Different scales have been addressed from the structural scale, see for instance [2–7, 10]; to models addressing more specifically smaller structures, structural details or parts of structures [11–13].

Different types of computational procedures or discretization were developed or applied to historical structures depending on the level of detail or the scales investigated. Finite element-based nonlinear solution procedures were used either combined with macroscopic continuum constitutive descriptions dealing with damage and plasticity as in [2–5, 14], or with an explicit description of the constituents (blocks or stones and mortar) [15]. Other contributions used Limit Analysis principles either based on finite element descriptions [7, 16] or based on block kinematics [17]. Discrete Elements frameworks were also exploited when descriptions intend to address the masonry texture [18, 19]. These advanced computational procedures are complemented by descriptions based on the definition of equivalent frames [20–22].

Loading conditions addressed in historic masonry structures modelling often relate to their seismic vulnerability. These were addressed by means of nonlinear static and dynamic procedures [3, 10, 20], or in contributions investigating the equivalence between both types of procedures [23]. Their relation to limit analysis and the investigation of specific pushover schemes were also addressed [7, 14, 21].

Most of the approaches having dealt with large scale structural analyses so far were mainly focused on periodic or quasi-periodic masonry in which continuous bed joints can be recognized [24–26]. The contributions dealing with irregular stone masonry structures with an explicit account for the constituents arrangement are less frequent. The effect of the arrangement (regular, irregular, rubble) was tested experimentally and modelled in [11]. More recently, homogenization methodologies have addressed the averaged behaviour of irregular stone masonry [17, 27–29].

Finally, an important aspect relates to the type of information used as input in modelling strategies used for historical masonry structures. In many instances, the structural models and investigations are fed by experimental observations, see for instance [6]. More recently, a significant effort by the community has been focusing on the extraction of input information on the geometry of masonry structures from images. Terrestrial Laser Scanning (TLS) point cloud information was used for health assessment of a minaret tower in [14]. TLS was also combined with IR thermography for historical buildings in [30], and was exploited in [31] for the extraction of brick shapes. Photogrammetry was also exploited to allow image-based modelling of masonry structures such as domes in [32]. The automation of model build-up based on images was developed based on the combination of image acquisition techniques (TLS and photogrammetry). Finite element macro-models were extracted based on machine learning techniques in [22], and Convolutional Neural Networks (CNNs) were also exploited to generate 2D digital twins in [33], and to produce segmentation tools for cracked masonry

structures modelling applied to regular masonry [34, 35].

The present contribution intends to address structural computations for ultimate limit states. When intending to address such states of masonry structures under various loading conditions, computational modelling is inherently challenging due to the material nonlinear behavior [11, 36], even when dealing with regular geometries, which results in macroscopic anisotropy and strength parameters that depend on the aspect ratio of blocks [37]. The geometric characteristics of irregular or rubble masonry render the evaluation of load transfer mechanisms even more complex [11, 38]. Consequently, to accurately model such structures, it is paramount to consider these irregular geometries as well as the contact and frictional behavior typically associated with masonry as a construction material [39].

Classically, full structural analysis is conducted using macroscopic models that focus on overall bulk behavior, treating the material as a homogeneous continuum [40, 41]. Defining an appropriate constitutive law at the macro-scale is key. To this end, homogenization proves useful [42–47], its goal being to identify equivalent macroscopic properties of masonry from the properties of the constituents and their geometrical arrangement, essentially linking meso to macro-scale, based on a Representative Volume Element [37, 46]. Although appealing, homogenization remains challenging as it must account for multiple elementary cells subjected to multiple loading conditions, each with different dimensions and positions within the structure for irregular masonry [29, 48–51]. Most models in the literature addressing non-periodic masonry rely on homogenization concepts [16, 21, 52]. They prove potent, but these averaging procedures fail to capture some failure modes properly.

Alternatively, masonry can be directly modeled at the mesoscopic scale. These models explicitly consider stacking modes and typically represent potential cracks as discrete interfaces, with positions assumed a priori, namely the mortar joints under the assumption of infinitely rigid or elastic blocks [53–56].

To date, the full-scale analysis of masonry structures using mesoscopic models has been strongly developed for regular masonry, where defining discrete cracking interfaces is relatively straightforward. Representing (potentially thicker) joints in irregular masonry remains however challenging, and current solutions lack sufficient computational efficiency to keep computation times reasonable [47]. A recent contribution addressed these issues on small masonry samples with a view to homogenization of failure properties based on images [17]. The present contribution aims to extend this numerically efficient methodology towards larger scale irregular masonry structures using a block-based Kinematic Limit Analysis procedure, leveraging a distance fields-based morphing procedure to lump mortar joints onto zero-thickness interfaces. To this end, it will be demonstrated that the efficiency of the proposed image-based Kinematic Limit Analysis procedure based on linear programming allows envisioning full structures computations. The limit criterion used in mortar joints used in [17] is enriched by considering additional failure modes with respect to a pure Mohr-Coulomb criterion (e.g. tension cut-off and compressive cap), and non proportional loading is accounted for to allow for pushover-like analyses with self weight. The procedure will be illustrated on 2D images of a facade from the church of the abbey of Preuilly, in Centre-Val de Loire, France; and an oil mill, in Bovina Marina, Italy.

The structure of this paper is organized as follows. We start by providing a comprehensive overview of the studied structures, emphasizing their historical context and structural properties, with a particular focus on block-stackings. Section 2 details the process for preparing the computational geometries. In Sect. 3, the Kinematic Limit Analysis procedure is presented along with the relevant theoretical developments. Section 4 discusses the assignment of loading configurations and material properties, followed by an analysis of the results in terms of load multipliers and failure mechanisms for both illustrative examples. Finally, in Sect. 5, we address the current limitations of the study, outline potential future developments, and revisit the assumptions necessary for applying this modeling strategy.

2 Geometry extraction and discretization

2.1 Abbey Church-Preuilly

The former Cistercian Abbey of Preuilly, located in the south of the French Department of

Seine-et-Marne, is not among the most famous of the Cîteaux's daughters. However, its founding date, 1116/1117, places it among the earliest of Cistercian expansion. The site was classified as a historical monument in 2004 [57].

Since the French Revolution, the abbey remained in the hands of the same family. Although not much remains of the abbey church, for which construction started in 1170, this continuity of ownership resulted in a well-documented history. From mid nineteenth century to the present day, several family members have been involved in the research on the history of the convent buildings [57].

Excavations have been limited to a few strategic locations. Geophysical surveys, field investigations, and other campaigns using modern techniques, among which lasergrammetry, have resulted in information useful to structural engineers, such as orthophotos, one of which will be used here to illustrate the proposed Kinematic Limit Analysis procedures. These orthophotos were initially meant as detailed stone-by-stone surveys with an indication of the type of stones and the regularly spaced putlog holes [57].

However, for the present contribution, these images can serve as the input for the suggested geometry extraction procedure and can be subsequently analyzed through Kinematic Limit Analysis. The first illustration of the method will use the interior part of the chancel end wall of the abbey church represented in Fig. 1.

In several zones, blocks were not identifiable due to factors such as plant growth. In these areas, one of the three following interventions was applied (Fig. 2): (i) ellipsoidal "blocks"were inserted in zones where rubble masonry using small blocks or covering plants were present, (ii) visible blocks from morphologically similar regions were copied and slightly altered and/or mirrored, and (iii) regular blocks were inserted, mainly in zones where the global geometry of the structure is delineated, such as the openings.

The assessed wall has dimensions of approximately 16 m in height and 10 m in width.

2.2 Oil Mill-Bovina Marina

The second illustrative structure is an oil mill that dates from the early twentieth century and is located between the San Pasquale river and Agrillei hill. It is taken from the homogenized limit analysis application presented in [16], and was first repeated in [58, 59]. The structure was constructed using traditional methods. The mill includes a 1.40 m high basement with 80 cm thick walls made from large stones and mortar, extending above ground as part of the foundation. The upper sections of the walls use a mix of smaller stones, brick pieces, and mortar, with small vertical clay brick ribs for structural regularity. The first floor comprises small brick vaults supported by old iron beams, and a timber truss structure, now heavily degraded, supports the roof [58, 59].

The walls were plastered and damaged in certain areas, as can be seen in Fig. 3. The present assessment adopts the same geometric arrangement proposed in [58, 59], where the irregular geometry of the walls was generated based on the approach outlined in these works.

The assessed wall is of dimensions 7.7 m in height and 6.6 m in width.

2.3 Computational geometry

A binarized image of the structure's blocks and joints serves as the primary input for a distance-field-based morphing procedure, for which the blocks serve as initial seeds. Prior to morphing, the unmorphed blocks must be properly identified and numbered [60]. This is achieved through geodesic image reconstruction. This method leverages the concept of geodesic paths; the shortest routes between points on a surface or curve, constrained by the topology of the image [61]. An initial marker point is randomly selected within a specified region of interest (the blocks) [62]. From this marker, geodesic paths to the surrounding pixels are traced, restricted by the binarized image, to support accurate reconstruction and facilitate the numbering of the blocks.

The morphing procedure was recently used in [17] for limit analysis-based homogenization.

The Fast Marching Method was employed to calculate the distance fields to the nearest neighboring blocks for each point on a regular rectangular grid [63]. A distance field, denoted here by DN_k, can be used to describe the packing state for the global block population by evaluating the distance at any point on the entire image to the k^{th} nearest block in the block set. For DN_1, positive distance values are attributed outside the block and negative values are given inside the block by convention [62].

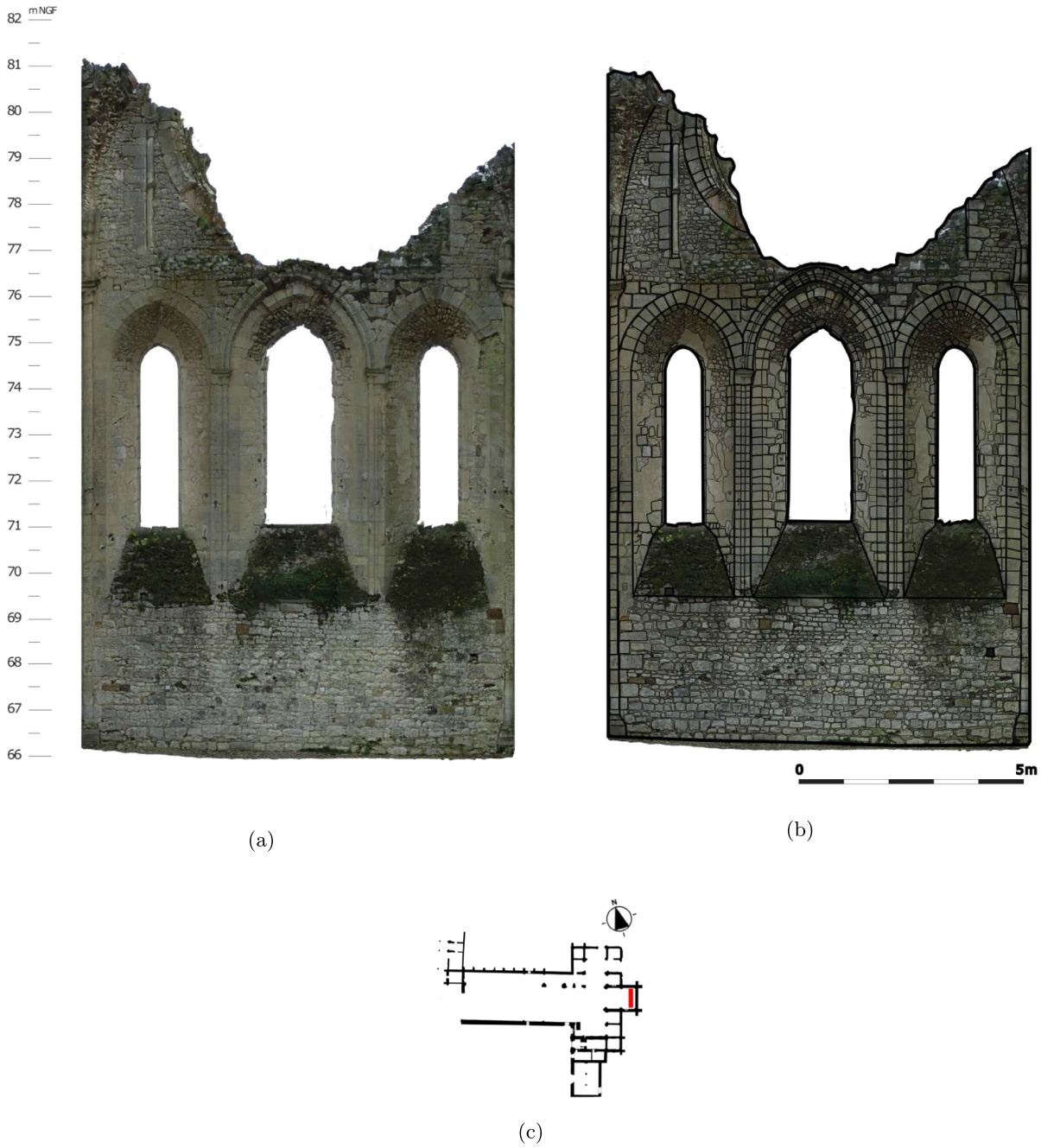

Fig. 1 **a** The orthophoto derived from lasergrammetry. **b** The orthophoto with block delineation. **c** Location of the wall relative to the abbey church indicated in red

The geometry of a set of neighboring blocks can be modified by manipulating these distance functions. A function that vanishes at the equidistant location between two nearest inclusions is defined as follows:

$$O_V(\mathbf{x}) = DN_2(\mathbf{x}) - DN_1(\mathbf{x}) \tag{1}$$

This function yields a morphing procedure that essentially morphs the shape of neighbouring bodies based on their interdistances, shapes, and size (Fig. 4).

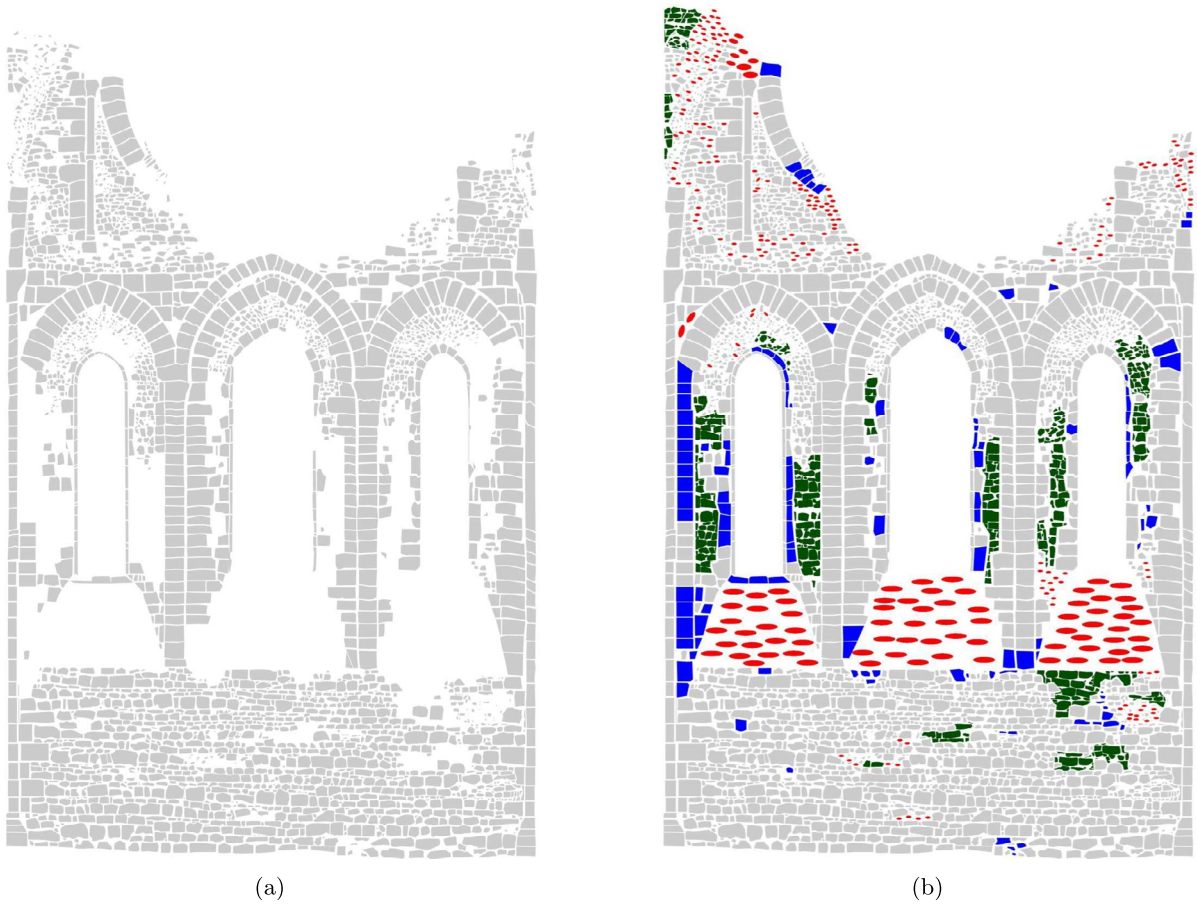

Fig. 2 **a** Blocks extracted from the orthophoto (Fig. 1). **b** With modifications. Red-ellipsoidal blocks inserted in zones where rubble masonry using small blocks or covering plant growth was present; Green-visible blocks from morphologically similar regions copied and slightly altered and/or mirrored; Blue-regular blocks, mainly in zones where the global geometry of the structure is delineated

Apart from masonry [17, 27, 56, 62], such functions have also been applied to describe geometries in other material contexts, including metallic foams [64, 65] and composites [66, 67]. The intrinsic dependence on the morphology of the global block arrangement constrains the final morphed geometry. For further details, the reader is diverted to [62].

The locus of points where O_V vanishes, i. e. the location where morphed blocks touch, defines the medial axis of the mortar joints. This concept is defined as the collection of points that have multiple closest points to the boundary of an object or a set of objects, also informally referred to as the image skeleton [68].

The extraction of the medial axis consists of a two-step approach as explained in [17]. The first step involves identifying triple junctions, which are points where the boundaries of three inter-block regions intersect, as defined by (1). This is achieved by evaluating the O_V-functions associated with each pair of blocks among the three. An initial guess point near the triple junction is iteratively displaced to the zero-level set of the corresponding O_V-functions defined for block pairs using their gradients. This procedure is stopped when the point aligns with the zero-level set of the O_V-functions given a prescribed accuracy. The medial axis is subsequently constructed by connecting the identified triple points by straight segments. The (optional) second step consists of further delineating the medial axis. To further discretize the straight segments connecting triple points, intermediate edge points are introduced between them. These

Fig. 3 North-wall of the structure. Image taken from [59]

edge points are then iteratively displaced to their correct positions using the O_V-functions and their gradients associated with the corresponding pairs of blocks.

This medial axis extraction procedure results in two computational geometry types; one with joints approximated as straight lines, and another with joints approximated as curved lines, as shown in Fig. 5 for the Abbey church of Preuilly and Fig. 6 for the oil-mill in Bovina Marina.

3 Limit analysis for rigid blocks

3.1 Upper bound formulation for infinitely rigid blocks

Consider an assembly of morphed blocks, where zero-thickness interfaces, simulating mortar joints, bring the blocks into direct contact with one another. A Kinematic Limit Analysis procedure will be established to ascertain the failure mechanism and the corresponding failure load. The masonry assembly is subjected to in-plane loading.

The deformations and failure within morphed blocks are prohibited by assuming infinitely rigid blocks. Therefore, the internal dissipation of power is only allowed along the interfaces. Classically, in limit analysis, an associated flow rule is assumed, inferring normality and a perfectly rigid plastic joint behavior is assigned. Furthermore, the small displacement kinematics assumption is included to linearize kinematics. The failure mechanism can be described by a discontinuous velocity field under these assumptions, representing the velocities of each block with corresponding discontinuities at interfaces.

By hypothesizing the blocks as infinitely resistant and stiff, the kinematics of each block can be described in a 2D problem through three quantities; two translational ($\dot{u}_x$ and $\dot{u}_y$) and one rotational ($\dot{\phi}_z$) degrees of freedom:

$$\dot{\mathbf{x}}_{k,j} = \left[\dot{u}_x, \dot{u}_y, \dot{\phi}_z\right]^{\mathrm{T}} \text{ for } j = 1, ..., N_E \tag{2}$$

Here, $\dot{\mathbf{x}}_{k,j}$ represents the degrees of freedom vector for the centroid of the j^{th} block. The components $\dot{u}_x$, $\dot{u}_y$, and $\dot{\phi}_z$ correspond to the translational and rotational velocities of the center of gravity G in the absolute reference frame. The total number of blocks in the assembly is denoted by N_E. The global vector of kinematic unknowns, $\dot{x}_k$, is constructed by assembling the degrees of freedom for all the blocks. Based on rigid body kinematics, the velocities at any point $\mathbf{P} = \left[x_P, y_P\right]^T$ on a block, corresponding to the i^{th} interface between blocks, can be expressed in relation to the centroid $\mathbf{G} = \left[x_G, y_G\right]^T$ of the block through a kinematic matrix. Assuming linearized kinematics, this relation is given as:

$$\begin{aligned} &\dot{\mathbf{u}}_P = \begin{bmatrix} \dot{u}_x^P \\ \dot{u}_y^P \end{bmatrix} = \mathbf{A}_G^P \dot{\mathbf{x}}_{k,i} \\ &\text{with } \mathbf{A}_G^P = \begin{bmatrix} 1 & 0 & -\left(y^P - y^G\right) \\ 0 & 1 & \left(x^P - x^G\right) \end{bmatrix} \end{aligned} \tag{3}$$

where $\dot{\mathbf{u}}_P = \left[\dot{u}_x^P, \dot{u}_y^P\right]$ are the velocities of point $\mathbf{P}$. $\mathbf{A}_G^P$ is the kinematic matrix associated with point $\mathbf{P}$ and centroid $\mathbf{G}$.

Geometric constraints (associated mechanically to the support conditions) are similarly defined by constraining velocity components of selected points, for example setting their velocity equal to zero.

The boundary of the admissible stress states domain, known as the yield surface $f(\boldsymbol{\sigma})$, is defined here as a Mohr-Coulomb surface with a tensile cut-off

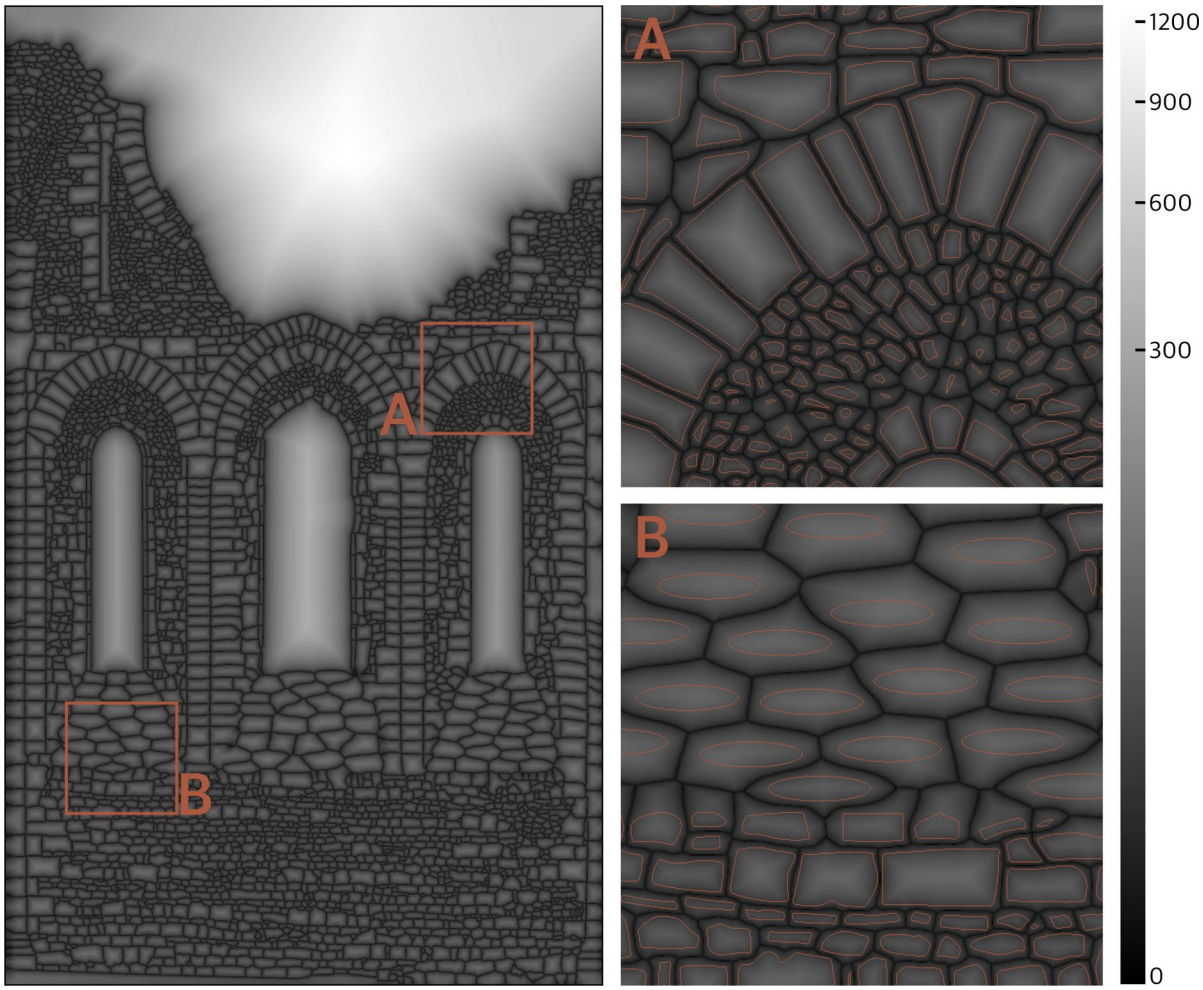

Fig. 4 The O_V function, as defined in Eq. 1, is illustrated. Two regions of interest are highlighted and labeled with boxes, indicating the areas zoomed in on the right. To enhance clarity, the outlines of the corresponding blocks in the zoomed-in sections are shown with colored contours

and a linearized compression cap. The associated flow rule is applied at the interfaces, and the related compatibility constraints are imposed. The associated flow rule infers normality, thus imposing that plastic strains evolve according to the normal to the yield surface. Plastic straining is represented by jumps in velocity:

$$\Delta\tilde{\mathbf{u}} = \mathbf{R}\Delta\dot{\mathbf{u}} = \dot{\lambda}\frac{\partial f}{\partial \boldsymbol{\sigma}} \text{ with } \mathbf{R} = \begin{bmatrix} \mathbf{n}^{\mathrm{T}} \\ \mathbf{s}^{\mathrm{T}} \end{bmatrix} \tag{4}$$

where $\Delta\tilde{\mathbf{u}}$ represents the velocity jump between two blocks at the interface, expressed in the local reference frame associated with the interface (indicated symbolically with a tilde $\tilde{}$). The symbol Δ denotes the difference in interface velocity between the blocks it connects. The matrix $\mathbf{R}$ comprises unit vectors that define the local coordinate system, which includes the unit normal vector $\mathbf{n}$ and the tangential vector $\mathbf{s}$ to the interface. The term $\dot{\lambda}$ denotes the plastic multiplier rates, which represent the rate at which plastic deformation occurs in response to the applied loads. The local frame of reference has been defined similarly to [17]. Note that plastic multiplier rates are not vectors. The bold symbol refers to the fact that there are multiple branches on the modified Mohr-Coulomb criterion:

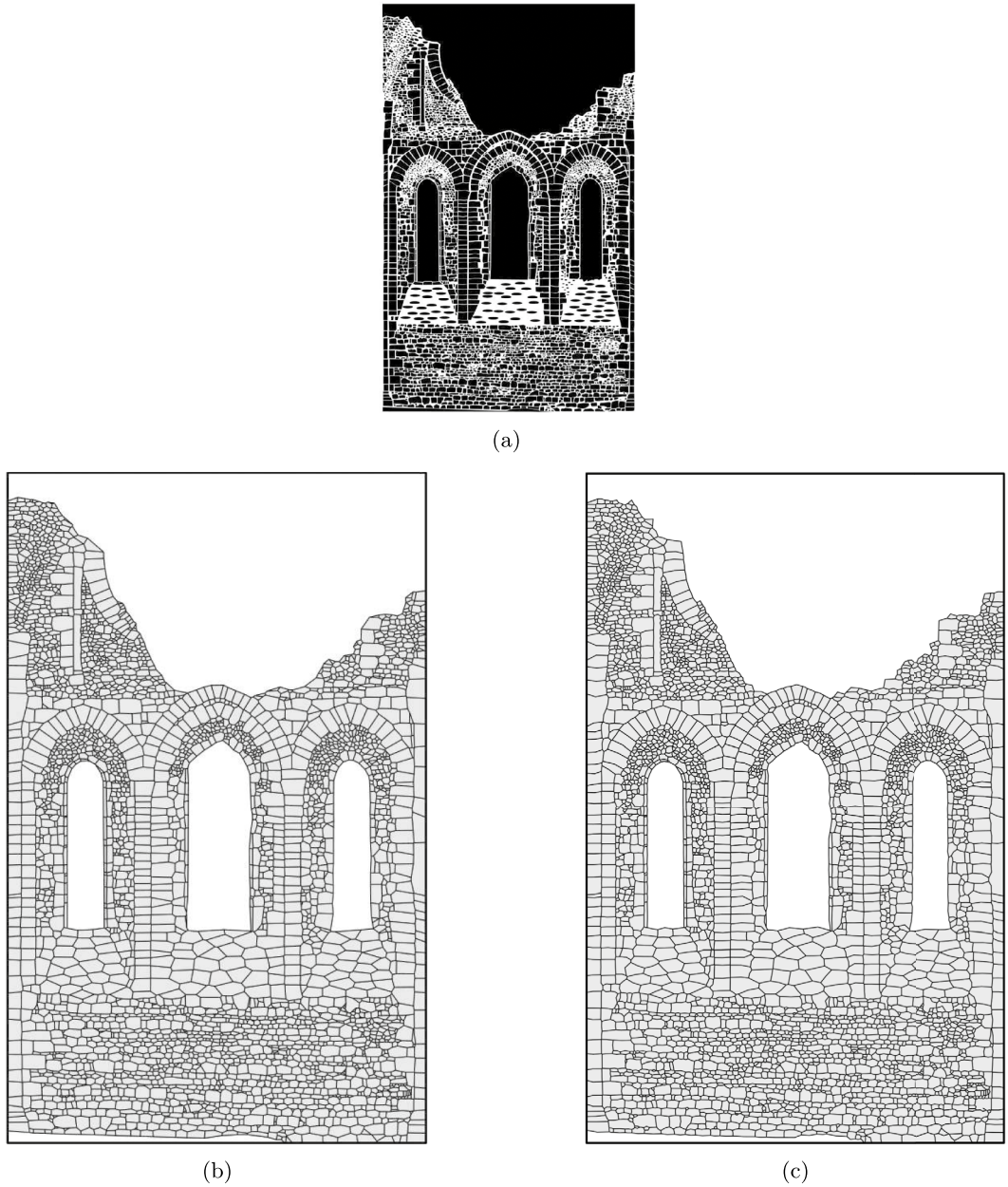

Fig. 5 **a** Image used as the input to the medial axis extraction tool for the abbey church. **b** The resulting straight-lined geometry. **c** The resulting curved-lined geometry. In the solution procedure, the gray blocks are considered active and the white blocks non-active, as discussed in Sect. 4.1

$$\Delta\tilde{\mathbf{u}} = \sum_{e=1}^{N_p} \dot{\lambda}_e \frac{\partial f_e}{\partial \boldsymbol{\sigma}} \tag{5}$$

where N_p indicates the number of branches on the assigned modified Mohr-Coulomb criterion. The plastic multiplier rates are subjected to the Kuhn-Tucker conditions to ensure the consistency of the plastic deformation [17].

The derivatives of the yield surface with respect to the stress are by definition normal to the branches used to define this surface. A linearization by

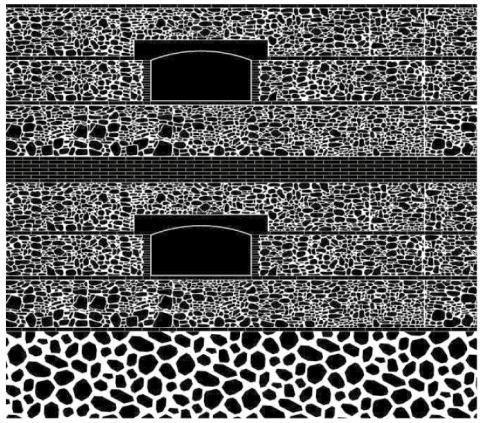

(a)

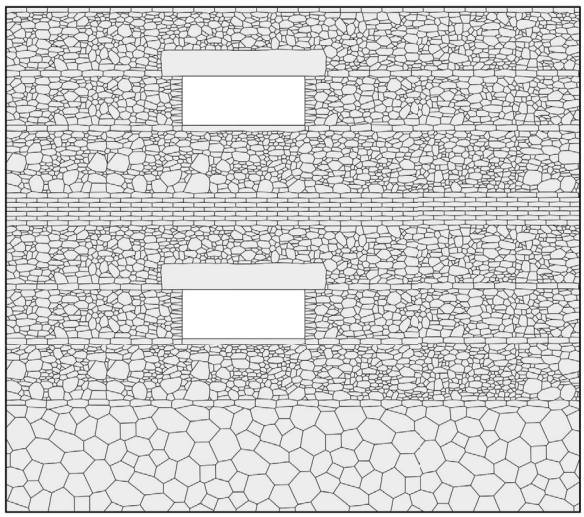

(b)

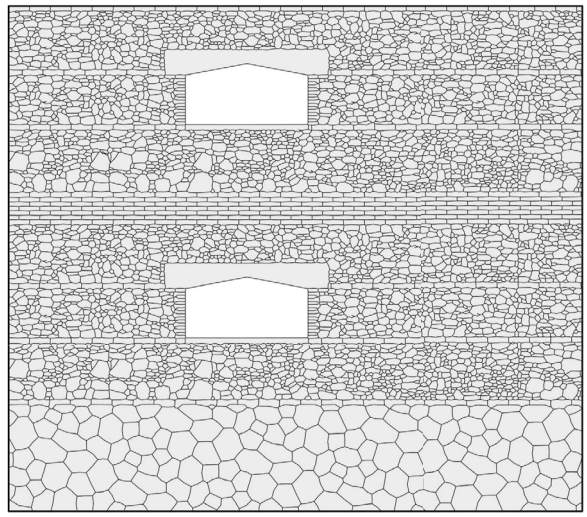

(c)

Fig. 6 **a** The image that serves as the input to the medial axis extraction tool for the oil mill. **b** The resulting straight-lined geometry. **c** The resulting curved-lined geometry. In the solution procedure, the gray blocks are considered active and the white blocks non-active, as discussed in Sect. 4.1

branches of the yield surface is required, analog to a linearization by planes for a yield surface formulated in 3D typically used to address out-of-plane loading conditions. The reader is referred to [41] for more details. The equation of each branch can be expressed as:

$$c_1\sigma + c_2\tau = c_0 \text{ such that } \sqrt{c_1^2 + c_2^2} = 1 \tag{6}$$

Therefore, the associative flow rule for the i^{th} point on an interface can be expressed as:

$$\dot{\boldsymbol{\lambda}}_i \frac{\partial f}{\partial \boldsymbol{\sigma}} = \sum_{e=1}^{N_p} \dot{\lambda}_{i,e} \begin{bmatrix} c_1 \\ c_2 \end{bmatrix}_e \tag{7}$$

The compatibility equation for one point on an interface can be constructed by combining Eq. (3), (4) and (7):

$$\mathbf{R}\left(\mathbf{A}^P_{G,\,j+1}\dot{\boldsymbol{x}}_{k,\,j+1} - \mathbf{A}^P_{G,\,j}\dot{\boldsymbol{x}}_{k,\,j}\right) - \sum_{e=1}^{N_p} \dot{\lambda}_{i,e} \begin{bmatrix} c_1 \\ c_2 \end{bmatrix}_e = \mathbf{0} \tag{8}$$

The limit load is assessed by the Principle of Virtual Power. Due to the assumption of a perfectly plastic material behavior, the internal power dissipation can be evaluated by summing the contributions over all the interfaces:

$$\begin{aligned} P_{in} &= \sum_{h=1}^{N_{int}} \int_{A_h} \tilde{\boldsymbol{\sigma}} \Delta \tilde{\dot{\mathbf{u}}} \, dA_h \\ &= \sum_{h=1}^{N_{int}} \int_{A_h} \tilde{\boldsymbol{\sigma}} \dot{\lambda} \frac{\partial f}{\partial \boldsymbol{\sigma}} dA_h \end{aligned} \tag{9}$$

with N_{int} the number of interfaces. A_h denotes the area of the h^{th} interface (considering the out-of-plane thickness of the interface), and $\tilde{\boldsymbol{\sigma}}$ the local stress vector. The internal power dissipation must be evaluated at each point of every interface:

$$\begin{aligned} P_{in} &= \sum_{h=1}^{N_{int}} \sum_{e=1}^{N_p} a_1 \dot{\lambda}_{1,e} \left[c_1 \sigma + c_2 \tau \right]_e \\ &\quad + a_2 \dot{\lambda}_{2,e} \left[c_1 \sigma + c_2 \tau \right]_e \\ &= \sum_{h=1}^{N_{int}} \sum_{e=1}^{N_p} \left(\dot{\lambda}_{1,e} c_{0e} \, l_h^{(1)} + \dot{\lambda}_{2,e} c_{0e} \, l_h^{(2)} \right) d \end{aligned} \tag{10}$$

where a_i denotes the area associated to the i^{th} point on the h^{th} interface. This can be replaced by the length l_h associated with points 1 and 2 of the interface (denoted by $^{(1)}$ and $^{(2)}$ respectively), which are the respective endpoints on the interface in question, multiplied by the depth of the assembly d. The reader is diverted to [17] and [41] for more information.

The power supplied by the externally applied loads is the total of the powers derived from their permanent and variable parts. In a general loading scenario, consider point loads $\mathbf{q}_P$, surface loads q_s and volume loads q_v:

$$\begin{aligned} P_{ext} = &\sum_i \mathbf{q}_{P,i} \dot{\mathbf{u}}_{P,i} + \int_S q_S \dot{\mathbf{u}} \, dS \\ &+ \int_V q_V \dot{\mathbf{u}} \, dV \end{aligned} \tag{11}$$

The assumption of rigid blocks allows this expression to be recast as a sum of resultant point loads multiplied by the corresponding velocities of the points of application, resulting in:

$$P_{ext} = \sum_k \mathbf{Q}_{P,k} \dot{\mathbf{u}}_{P,k} \tag{12}$$

with $\mathbf{Q}_{P,\,k}$ the k^{th} load resultant applied to the k^{th} point of application $\mathbf{P}_k$.

The permanent loads $\mathbf{Q}_{perm}$ can be distinguished from the variable loads $\mathbf{Q}_\lambda = \lambda \mathbf{Q}_{var}$, with λ the load multiplier. Thus, the externally supplied power can be expressed as:

$$\begin{aligned} P_{ext} = &\sum_{k_{perm}} \mathbf{Q}_{perm,\,k_{perm}} \dot{\mathbf{u}}_{P,\,k_{perm}} \\ &+ \lambda \sum_{k_{var}} \mathbf{Q}_{var,\,k_{var}} \dot{\mathbf{u}}_{P,\,k_{var}} \end{aligned} \tag{13}$$

Based on the classical Kinematic Limit Analysis assumptions, the power resulting from variable loads is linearly dependent on the load multiplier. A normalization condition is imposed to restrict self-similar failure mechanisms to one:

$$P_{ext,var} = \sum_{k_{var}} \mathbf{Q}_{var,\,k_{var}} \dot{\mathbf{u}}_{P,\,k_{var}} = 1 \tag{14}$$

The Principle of Virtual Power states that the internal power dissipation should balance the externally supplied power. The load multiplier can therefore be determined as follows:

$$\begin{aligned} &P_{in} = P_{ext,\,perm} + \lambda P_{ext,\,var} \\ &\iff \lambda = \frac{P_{in} - P_{ext,\,perm}}{P_{ext,\,var}} \end{aligned} \tag{15}$$

Thus by combining Eq. (9) and (10), the equation determining the load multiplier may be expressed as:

$$\begin{aligned} \lambda = &\sum_{h=1}^{N_{int}} \sum_{e=1}^{N_p} \left(\dot{\lambda}_{1,e} c_{0e} \, l_h^{(1)} + \dot{\lambda}_{2,e} c_{0e} \, l_h^{(2)} \right) d \\ &- \sum_{k_{perm}} \mathbf{Q}_{perm,\,k_{perm}} \dot{\mathbf{u}}_{P,\,k_{perm}} \end{aligned} \tag{16}$$

λ depends linearly on the kinematic unknowns and plastic multiplier rates, bundled in the global vector of unknowns $\mathbf{x} = \left[\dot{\mathbf{x}}_k, \dot{\lambda} \right]$. The solution is obtained by solving a minimization problem, which is formulated in its canonical form:

$$\begin{aligned} &\text{minimize} \quad \lambda = \mathbf{c}^{\mathrm{T}} \mathbf{x} \\ &\text{subject to} \quad \mathbf{A}^{global} \mathbf{x} = \mathbf{b} \\ &\qquad\qquad \dot{\lambda} \geq \mathbf{0} \end{aligned} \tag{17}$$

resulting in the discontinuous velocity field that minimizes λ under the imposed geometric, compatibility, and normalization constraints, bundled in $\mathbf{A}^{global}$. The plastic multiplier rates should assume non-negative values. $\mathbf{b}$ is the vector of known terms in the equality equations and $\mathbf{c}$ the vector of coefficients such that $P_{in} = \mathbf{c}^{\mathrm{T}} \mathbf{x}$.

The final problem is formulated as a sparse linear programming problem and is solved using SciPy's

linprog function, which implements a pivot-based algorithm, as described in [69].

4 Results and discussion

4.1 Loading configuration and material properties

The straight-lined and curved-lined geometries of the two structures, shown in Figs. 5 and 6, were subjected to push-over-like loading conditions. A linearly varying load in terms of the position in height is applied to both the left and right sides of the structures (also respectively referred to as scheme L and scheme R), as illustrated in Figs. 8, 9, 10 and 11. A dead load consistent with the self-weight was also applied, accounting for a block density of 2200 kg/m^3. The assigned wall thicknesses are 0.5 m and 0.8 m for the abbey church and oil mill respectively.

In both cases, the mortar joints were characterized by material properties matching a modified Mohr-Cloumb criterion, incorporating a compression cap and tensile cut-off, as depicted in Fig. 7. The material parameters used are detailed in Table 1.

Blocks can be selectively activated or deactivated by disregarding the corresponding interfaces, essentially treating them as voids. This method has been applied to specific blocks: the openings, and concerning the abbey church the top block defining the distinct outline of the ruins, and the bottom block, which compensates for the uneven soil beneath.

The number of blocks, interfaces, and unknowns for each loading case is provided in Table 2. The computation time ranges from approximately five minutes for the straight-lined geometries to around one hour for the curved-lined geometries, using a non-commercial linear programming solver.

4.2 Results-load multipliers

The load multipliers corresponding to their respective failure mechanisms are presented in Table 3.

Table 1 Material parameters assigned to the joints. The parameters correspond with Fig. 7

f_c [MPa]	2.5	θ [°]	30
f_t [MPa]	0.1	α [°]	45
c [kPa]	140		

Table 2 Number of blocks, interfaces and unknowns for each case study

Oil Mill	Straight-Lined	Curved-Lined
# Blocks	4907	4935
# Interfaces	14557	29143
# Unknowns	305861	597665
Abbey	**Straight-Lined**	**Curved-Lined**
# Blocks	3539	3545
# Interfaces	10284	20590
# Unknowns	216297	422435

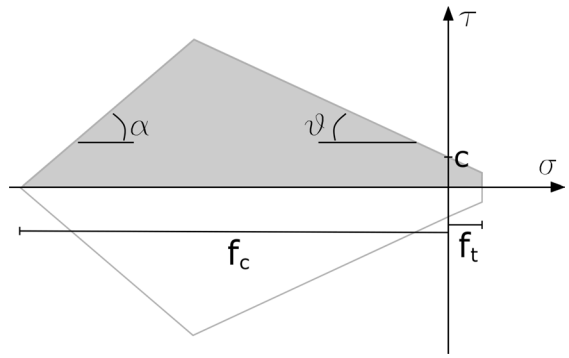

Fig. 7 Modified Mohr-Coulomb criterion with compression cap and tensile cut-off assigned to the interfaces

Although the multiplier rates are comparable, the curved-line geometries show higher values. This observation aligns with the findings reported in [17], and which may be related to the increased mechanical interlocking for curved joints.

4.3 Failure mechanisms abbey church-preuilly

Consistent with expectations, failure occurs around the window openings, evidenced by significant horizontal cracks. The increased height on the left side of the structure acts as a lever arm, resulting in a lower load multiplier required to induce failure for loading scheme L compared to loading scheme R. This is also observed in the normalized load multipliers, in Table 3.

The failure mechanisms for both straight-lined and curved-lined geometries are largely consistent, though some slight differences are observable. For scheme L, shown in Fig. 8, crack pattern F shows a single horizontal crack in the rubble zone around

Table 3 The results in terms of load multiplier λ for each loading case, and the resultant load multiplier normalized $\bar{\lambda}$ with respect to the dead loads (the structure's self-weight). C and O refer to the abbey church and the oil mill respectively

Scheme	λ [kN/m]		$\bar{\lambda}$ [-]	
	Straight	Curved	Straight	Curved
L C	211.935	217.064	1.404	1.437
R C	273.256	283.416	1.809	1.877
L O	531.804	546.526	2.085	2.154
R O	583.899	609.111	2.231	2.402

the window opening for the curved-lined geometry, whereas the straight-lined geometry exhibits a double crack in this area. For scheme R, shown in Fig. 9, crack pattern F is very similar for both geometries, though a larger zone is activated in the straight-lined case.

4.4 Failure mechanisms Oil Mill-Bovina Marina

For both loading configurations (Figs. 10 and 11), two types of cracks occur; straight horizontal cracks and diagonal cracks. They either originate/terminate in one another, or in the openings. On the loaded edge, large horizontal cracks form in the bed joints of the regular bricks, either terminating at the openings or extending into diagonal cracks. This results in a wedge-like failure pattern, consistent with expectations given the applied loading conditions.

The failure mechanisms for both straight and curved-lined geometries are similar. However, under loading scheme L, the straight-lined geometry exhibits an additional diagonal crack, as illustrated in Fig. 10. This diagonal crack is not present in the curved-lined geometry. Although subtle, the cracking pattern A for the oil mill subjected to loading scheme R shows a difference: the straight-lined geometry has a small diagonal crack near the window opening, while the curved-lined geometry shows an additional diagonal crack approximately in the center of the large horizontal crack.

5 Conclusions and outlook

In the present work, a computationally efficient method for evaluating irregular unreinforced

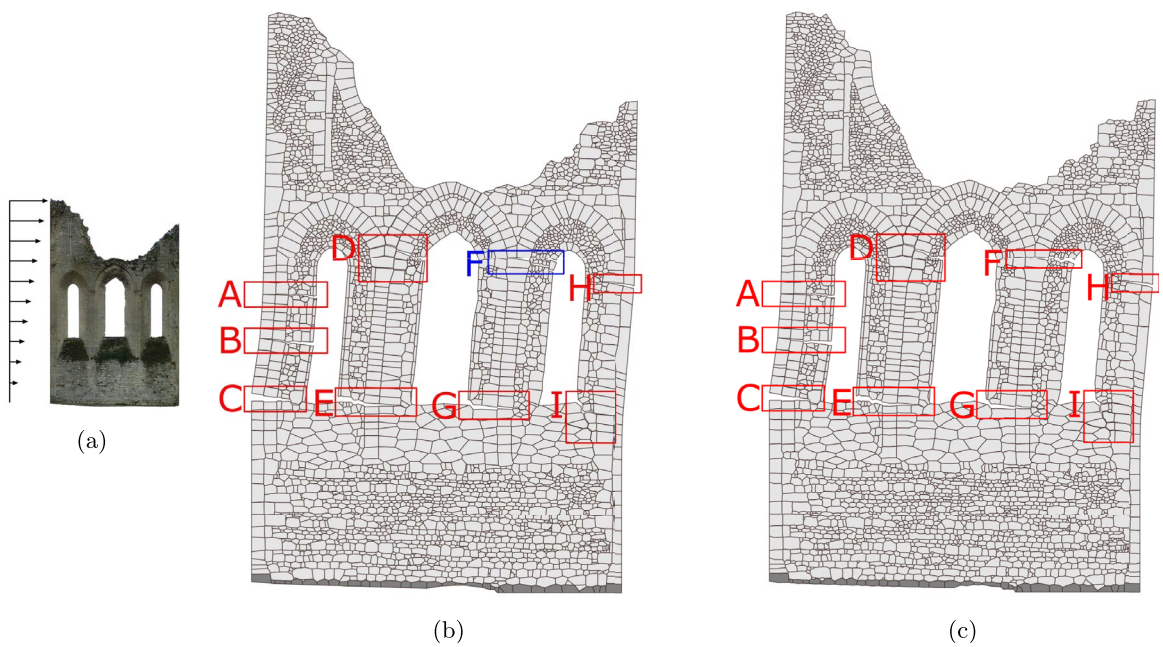

Fig. 8 **a** Loading scheme applied to the abbey church - a triangular load applied along the full left side of the structure. **b** Resulting failure mode for the straight-lined representative computational geometry. **c** Resulting failure mode for the curved-lined representative computational geometry. The dark gray blocks represent blocks that are fixed. Cracking locations are annotated through labeled red and blue boxes

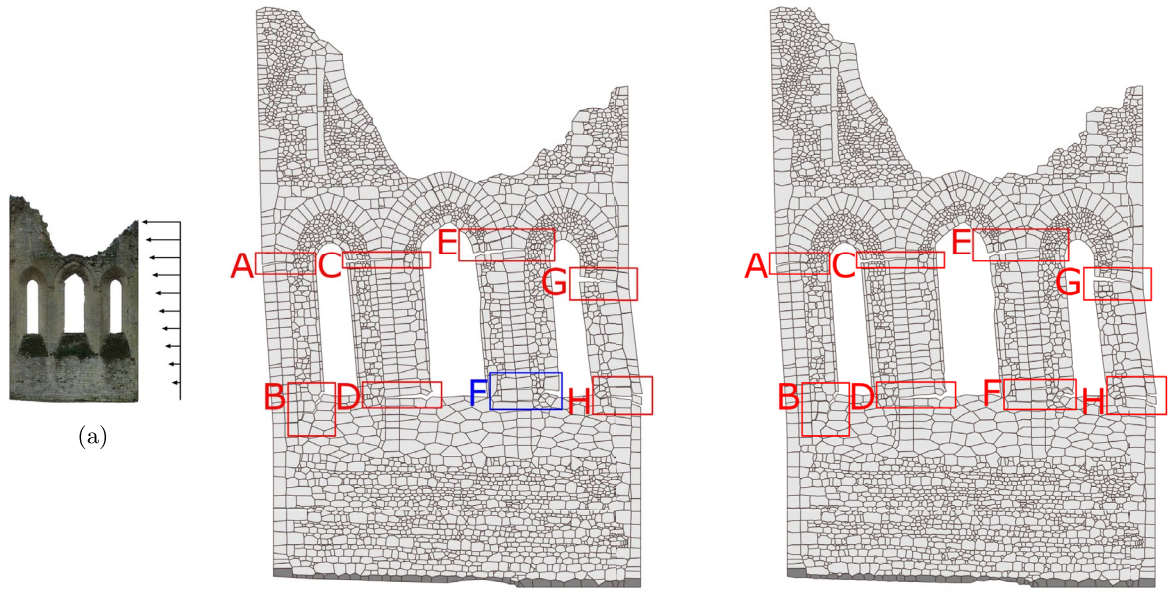

Fig. 9 **a** Loading scheme applied to the abbey church - a triangular load applied along the full right side of the structure. **b** Resulting failure mode for the straight-lined representative computational geometry. **c** Resulting failure mode for the curved-lined representative computational geometry. The dark gray blocks represent blocks that are fixed. Cracking locations are annotated through labeled red and blue boxes

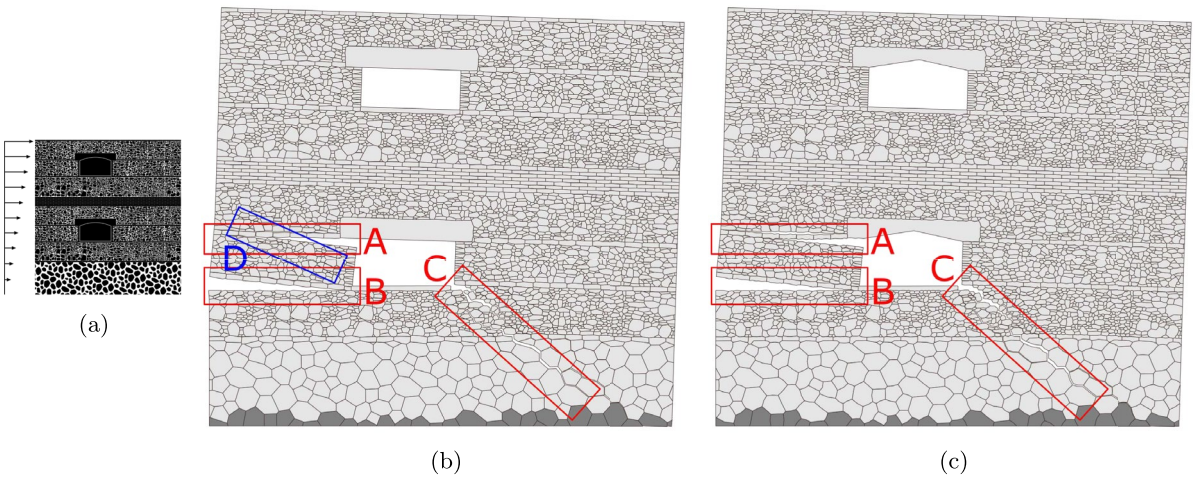

Fig. 10 **a** Loading scheme applied to the oil mill - a triangular load applied along the full right side of the structure. **b** Resulting failure mode for the straight-lined representative computational geometry. **c** Resulting failure mode for the curved-lined representative computational geometry. The dark gray blocks represent blocks that are fixed. Cracking locations are annotated through labeled red and blue boxes

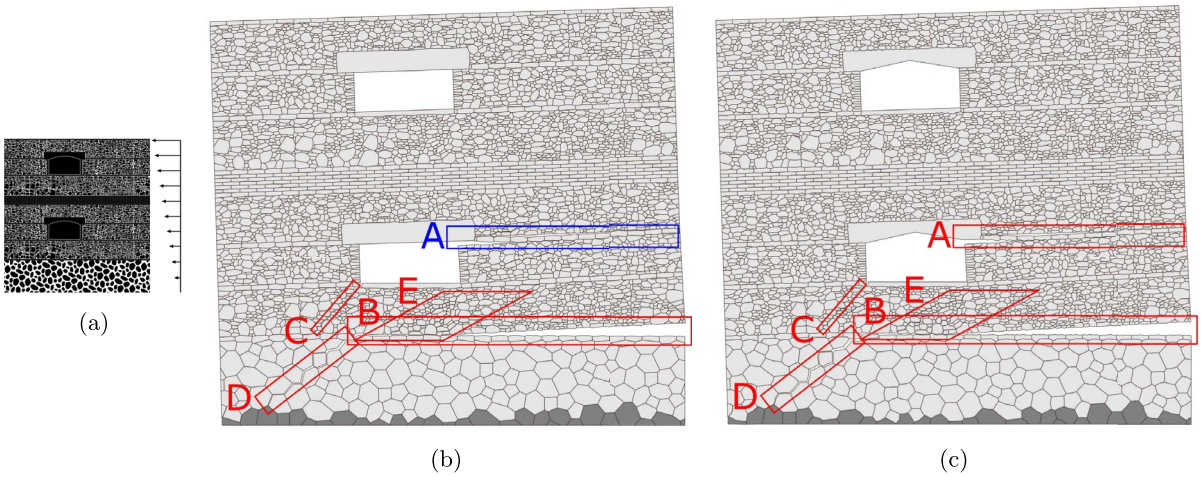

Fig. 11 **a** Loading scheme applied to the oil mill - a triangular load applied along the full right side of the structure. **b** Resulting failure mode for the straight-lined representative computational geometry. **c** Resulting failure mode for the curved-lined representative computational geometry. The dark gray blocks represent blocks that are fixed. Cracking locations are annotated through labeled red and blue boxes

historic masonry has been developed, with the capability to explicitly consider the structure's stacking patterns.

This methodology was demonstrated using two case studies: the assessment of the east-facing wall of the Abbey of Preuilly and the assessment of an oil mill in Bovina Marina.

To determine the computational geometry of the abbey church, blocks were extracted from an orthophoto, and in areas where block delineation was challenging, one of three interventions was employed to create a representative geometry: (i) insertion of ellipsoidal blocks subsequently morphed by the distance field approach, (ii) duplication and/or slight alteration of blocks from morphologically similar regions, and (iii) insertion of regular-like blocks in zones where the overall features of the structure are outlined.

Since the walls of the oil mill are plastered, a computationally generated geometry was assumed. The corresponding geometry was taken from [58] and [59].

A distance field-based morphing operation was used to represent mortar joints as zero-thickness interfaces, with optional user-defined refinement. This equivalent geometry was then analyzed using a Kinematic Limit Analysis procedure, assuming the blocks to be infinitely stiff and strong, and assigning a modified Mohr-coulomb behavior to the joints. The limit analysis problem was solved using linear programming.

The failure mechanisms for both straight-lined and curved-lined geometries exhibit overall consistency, though some slight distinctions are notable. In the case of the Abbey Church at Preuilly, under loading scheme L, the curved-lined geometry shows a single horizontal crack around the window opening, whereas the straight-lined geometry presents a double crack in the same area. For loading scheme R, the failure patterns are similar, with the straight-lined geometry activating a larger zone. At the Oil Mill in Bovina Marina, the straight-lined geometry under loading scheme L features both horizontal and smaller diagonal cracks, whereas the curved-lined geometry lacks the diagonal crack, highlighting a key difference between the two geometries. The similarity is also reflected in the value of the load-multiplier rates. Results are consistent with [17] - straight-lined geometries exhibit a slightly smaller load multiplier, as less interlocking between blocks can occur.

Future developments will focus on addressing non-identifiable zones through local meshing techniques, potentially combined with homogenization. Additional advancements will include evaluating three-dimensional geometries and loading schemes, under the assumption of single-leaf masonry, where extrusion in the depth direction is a viable approach. Given

that the computational cost and the time required for solving the final systems for the straight-lined and curved-lined geometries are relatively low, the developed code was not optimized, non-commercial solvers were used, and all computations were addressed on a standard laptop. Further developments addressing three-dimensional geometries appear feasible, as long as the structures studied are not extraordinarily large.

Acknowledgements The first author gratefully acknowledges the support of the Fonds de la Recherche Scientifique – FNRS – Communauté française de Belgique through the funding of a FRIA grant under grant number 40021962. The second author gratefully acknowledges the support of the Fonds de la Recherche Scientifique – FNRS – Communauté française de Belgique through the postdoctoral grant "Chargé de Recherche" under grant no. 40010864.

Declarations

Conflict of interest The authors declare that they have no known competing financial interests or personal relationships that could have appeared to influence the work reported in this paper.

References

1. Spence R, Foulser-Piggott R, Pomonis A, Crowley H, Gueguen P, Masi A, Chiauzzi L, Zuccaro G, Cacace F, Zulfikar C, Markus M, Schaefer D, Sousa M, Kappos A (2012) The european building stock inventory: creating and validating a uniform database for earthquake risk modelling, Lisboa, Portugal, pp. 1–10. Paper presented at the 15th World Conference on Earthquake Engineering
2. Saloustros S, Pelà L, Roca P, Portal J (2015) Numerical analysis of structural damage in the church of the poblet monastery. Eng Fail Anal 48:41–61. https://doi.org/10.1016/j.engfailanal.2014.10.015
3. Valente M, Milani G (2019) Damage assessment and collapse investigation of three historical masonry palaces under seismic actions. Eng Fail Anal 98:10–37. https://doi.org/10.1016/j.engfailanal.2019.01.066
4. Roca P, Cervera M, Pelà L, Clemente R, Chiumenti M (2013) Continuum fe models for the analysis of mallorca cathedral. Eng Struct 46:653–670. https://doi.org/10.1016/j.engstruct.2012.08.005
5. Lourenço PB, Krakowiak KJ, Fernandes FM, Ramos LF (2007) Failure analysis of monastery of jeronimos, lisbon: How to learn from sophisticated numerical models. Eng Fail Anal 14:280–300. https://doi.org/10.1016/j.engfailanal.2006.02.002
6. Ciocci MP, Sharma S, Lourenço PB (2018) Engineering simulations of a super-complex cultural heritage building: Ica cathedral in Peru. Meccanica 53:1931–1958. https://doi.org/10.1007/s11012-017-0720-3
7. Milani G, Valente M (2015) Comparative pushover and limit analyses on seven masonry churches damaged by the 2012 emilia-romagna (italy) seismic events: Possibilities of non-linear finite elements compared with pre-assigned failure mechanisms. Eng Fail Anal 47:129–161. https://doi.org/10.1016/j.engfailanal.2014.09.016
8. Roca P, Cervera M, Gariup G, Pela L (2010) Structural analysis of masonry historical constructions. classical and advanced approaches. Arch Comput Methods Eng 17:299–325. https://doi.org/10.1007/s11831-010-9046-1
9. Lourenço PB (2002) Computations on historic masonry structures. Prog Struct Mat Eng 4:301–319. https://doi.org/10.1002/pse.120
10. Betti M, Vignoli A (2008) Modelling and analysis of a romanesque church under earthquake loading: assessment of seismic resistance. Eng Struct 30(2):352–367. https://doi.org/10.1016/j.engstruct.2007.03.027
11. Senthivel R, Lourenço PB (2009) Finite element modelling of deformation characteristics of historical stone masonry shear walls. Eng Struct 31(9):1930–1943. https://doi.org/10.1016/j.engstruct.2009.02.046
12. Psycharis IN, Lemos JV, Papastamatiou DY, Zambas C, Papantonopoulos C (2003) Numerical study of the seismic behaviour of a part of the parthenon pronaos. Earthq Eng Struct Dyn 32(13):2063–2084. https://doi.org/10.1002/eqe.315
13. Pegon P, Pinto AV, Géradin M (2001) Numerical modelling of stone-block monumental structures. Comput Struct 79(22):2165–2181. https://doi.org/10.1016/S0045-7949(01)00070-0
14. Korumaz M, Betti M, Conti A, Tucci G, Bartoli G, Bonora V, Korumaz AG, Fiorini L (2017) An integrated terrestrial laser scanner (tls), deviation analysis (da) and finite element (fe) approach for health assessment of historical structures. a minaret case study. Eng Struct 153:224–238. https://doi.org/10.1016/j.engstruct.2017.10.026
15. Pereira M, D'Altri AM, de Miranda S, Glisic B (2023) Automatic multi-leaf nonperiodic block-by-block pattern generation and computational analysis of historical masonry structures. Eng Struct 283:115945. https://doi.org/10.1016/j.engstruct.2023.115945
16. Milani G, Esquivel YW, Lourenço PB, Riveiro B, Oliveira DV (2013) Characterization of the response of quasi-periodic masonry: Geometrical investigation, homogenization and application to the guimarães castle, portugal. Eng Struct 56:621–641. https://doi.org/10.1016/j.engstruct.2013.05.040
17. Hermans YFL, Grillanda N, Ehab Moustafa Kamel K, Milani G, Massart TJ (2024) Efficient image-based homogenized limit analysis for irregular masonry with lumped mortar joints representation. Eng Struct 318:118688. https://doi.org/10.1016/j.engstruct.2024.118688
18. Abu-Haifa M, Lee SJ (2023) Image-based 3d modeling-to-simulation of single-wythe masonry structure via reverse descriptive geometry. J Build Eng 76:107125. https://doi.org/10.1016/j.jobe.2023.107125
19. Giordano A, Mele E, Luca AD (2002) Modelling of historical masonry structures: comparison of different approaches through a case study. Eng Struct 24:1057–1069. https://doi.org/10.1016/S0141-0296(02)00033-0

20. Clementi F, Gazzani V, Poiani M, Lenci S (2016) Assessment of seismic behaviour of heritage masonry buildings using numerical modelling. J Build Eng 8:29–47. https://doi.org/10.1016/j.jobe.2016.09.005
21. Cundari GA, Milani G (2013) Homogenized and heterogeneous limit analysis model for pushover analysis of ancient masonry walls with irregular texture. Int J Arch Heritage 7(3):303–338. https://doi.org/10.1080/15583058.2011.640737
22. Pantoja-Rosero BG, Achanta R, Beyer K (2024) Automated image-based generation of finite element models for masonry buildings. Bull Earthq Eng 22:3441–3469. https://doi.org/10.1007/s10518-023-01726-7
23. Endo Y, Pelà L, Roca P (2017) Review of different pushover analysis methods applied to masonry buildings and comparison with nonlinear dynamic analysis. J Earthquake Eng 21(8):1234–1255. https://doi.org/10.1080/13632469.2016.1210055
24. Szabó S, Funari MF, Lourenço PB (2024) A mason-inspired pattern generator for historic masonry structures using quality indexes. Eng Struct 304:117604. https://doi.org/10.1016/j.engstruct.2024.117604
25. Portioli F, Casapulla C, Gilbert M, Cascini L (2014) Limit analysis of 3d masonry block structures with non-associative frictional joints using cone programming. Comput Struct 143:108–121. https://doi.org/10.1016/j.compstruc.2014.07.010
26. Lucrezia Cascini RG, Portioli F (2020) Liablock_3d: a software tool for collapse mechanism analysis of historic masonry structures. Int J Arch Heritage 14(1):75–94. https://doi.org/10.1080/15583058.2018.1509155
27. Ehab Moustafa Kamel K, Massart TJ, Sonon B (2018) Level set-based generation of representative volume elements for the damage analysis of irregular masonry. Meccanica 53:1737–1755. https://doi.org/10.1007/s11012-017-0695-0
28. Krejčí T, Koudelka T, Bernardo V, Šejnoha M (2021) Effective elastic and fracture properties of regular and irregular masonry from nonlinear homogenization. Comput Struct 254:106580. https://doi.org/10.1016/j.compstruc.2021.106580
29. Cavalagli N, Cluni F, Gusella V (2018) Failure surface of quasi-periodic masonry by means of statistically equivalent periodic unit cell approach. Meccanica 53(7):1719–1736. https://doi.org/10.1007/s11012-017-0771-5
30. Costanzo A, Minasi M, Casula G, Musacchio M, Buongiorno MF (2015) Combined use of terrestrial laser scanning and ir thermography applied to a historical building. Sensors 15(1):194–213. https://doi.org/10.3390/s150100194
31. Shen Y, Wang J, Wei S, Zheng D, Ferreira VG (2019) Accurate extraction of brick shapes in masonry walls from dense terrestrial laser scanning point cloud. Measurement 146:254–267. https://doi.org/10.1016/j.measurement.2019.05.086
32. Sánchez-Aparicio LJ, Villarino A, García-Gago J, González-Aguilera D (2015) Non-contact photogrammetric methodology to evaluate the structural health of historical constructions. In: The International Archives of the Photogrammetry, Remote Sensing and Spatial Information Sciences XL-5/W4, pp 331–338 https://doi.org/10.5194/isprsarchives-XL-5-W4-331-2015
33. Loverdos D, Sarhosis V (2023) Image2dem: a geometrical digital twin generator for the detailed structural analysis of existing masonry infrastructure stock. SoftwareX 22:101323. https://doi.org/10.1016/j.softx.2023.101323
34. Loverdos D, Sarhosis V, Adamopoulos E, Drougkas A (2021) An innovative image processing-based framework for the numerical modelling of cracked masonry structures. Autom Constr 125:103633. https://doi.org/10.1016/j.autcon.2021.103633
35. Loverdos D, Sarhosis V (2022) Automatic image-based brick segmentation and crack detection of masonry walls using machine learning. Autom Constr 140:104389. https://doi.org/10.1016/j.autcon.2022.104389
36. Lourenco PB (1996) Computational strategies for masonry structures. Doctoral thesis, Civil Engineering and Geosciences, Delft University of Technology
37. de Buhan P, de Felice G (1997) A homogenization approach to the ultimate strength of brick masonry. J Mech Phys Solids 45(7):1085–1104. https://doi.org/10.1016/S0022-5096(97)00002-1
38. Šejnoha J, Šejnoha M, Zeman J, Sýkora J, Vorel J (2008) Mesoscopic study on historic masonry. Struct Eng Mech 30:99–117. https://doi.org/10.12989/SEM.2008.30.1.099
39. Livesley RK (1978) Limit analysis of structures formed from rigid blocks. Int J Numer Meth Eng 12(12):1853–1871. https://doi.org/10.1002/nme.1620121207
40. Grillanda N, Valente M, Milani G (2020) Anub-aggregates: a fully automatic nurbs-based software for advanced local failure analyses of historical masonry aggregates. Bull Earthq Eng 18:3935–3961. https://doi.org/10.1007/s10518-020-00848-6
41. Grillanda N, Chiozzi A, Milani G, Tralli A (2022) Nurbs solid modeling for the three-dimensional limit analysis of curved rigid block structures. Comput Methods Appl Mech Eng 399:115304. https://doi.org/10.1016/j.cma.2022.115304
42. Milani G, Lourenço P (2010) Monte carlo homogenized limit analysis model for randomly assembled blocks in-plane loaded. Comput Mech 46:827–849. https://doi.org/10.1007/s00466-010-0514-0
43. Milani G, Lourenço PB (2010) A simplified homogenized limit analysis model for randomly assembled blocks out-of-plane loaded. Comput Struct 88(11):690–717. https://doi.org/10.1016/j.compstruc.2010.02.009
44. Milani G (2011) Simple lower bound limit analysis homogenization model for in- and out-of-plane loaded masonry walls. Constr Build Mater 25(12):4426–4443. https://doi.org/10.1016/j.conbuildmat.2011.01.012
45. Pande GN, Liang JX, Middleton J (1989) Equivalent elastic moduli for brick masonry. Comput Geotech 8(3):243–265. https://doi.org/10.1016/0266-352X(89)90045-1
46. Suquet P (1983) Analyse limite et homogeneisation. Comptes Rendus de l'Academie des Sciences - Series IIB -Mechanics 296:1355–1358
47. Tiberti S, Milani G (2019) 2d pixel homogenized limit analysis of non-periodic masonry walls. Comput Struct 219:16–57. https://doi.org/10.1016/j.compstruc.2019.04.002

48. Cluni F, Gusella V (2004) Homogenization of non-periodic masonry structures. Int J Solids Struct 41(7):1911–1923. https://doi.org/10.1016/j.ijsolstr.2003.11.011
49. Cavalagli N, Cluni F, Gusella V (2013) Evaluation of a statistically equivalent periodic unit cell for a quasi-periodic masonry. Int J Solids Struct 50(25):4226–4240. https://doi.org/10.1016/j.ijsolstr.2013.08.027
50. Gitman IM, Askes H, Sluys LJ (2007) Representative volume: existence and size determination. Eng Fract Mech 74(16):2518–2534. https://doi.org/10.1016/j.engfracmech.2006.12.021
51. Mercatoris B, Massart TJ (2009) Assessment of periodic homogenization-based multiscale computational schemes for quasi-brittle structural failure. Int J Multiscale Comput Eng 7(2):153–170. https://doi.org/10.1615/IntJMultCompEng.v7.i2.60
52. Valentino J, Gilbert M, Gueguin M, Smith CC (2023) Limit analysis of masonry walls using discontinuity layout optimization and homogenization. Int J Numer Meth Eng 124(2):358–381. https://doi.org/10.1002/nme.7124
53. Lotfi HR, Shing PB (1994) Interface model applied to fracture of masonry structures. J Struct Eng-ASCE 120(1):63–80. https://doi.org/10.1061/(ASCE)0733-9445(1994)120:1(63)
54. Lourenço PB, Rots JG (1997) Multisurface interface model for analysis of masonry structures. J Eng Mech 123(7):660–668. https://doi.org/10.1061/(ASCE)0733-9399(1997)123:7(660)
55. Alfano G, Sacco E (2006) Combining interface damage and friction in a cohesive-zone model. Int J Numer Meth Eng 68(5):542–582. https://doi.org/10.1002/nme.1728
56. Hermans YFL, Grillanda N, Ehab Moustafa Kamel K, Milani G, Massart TJ (2024) Image-Based kinematic limit analysis for historic masonry with zero-thickness mortar joints. In:Milani G, Ghiassi B (eds) IB2MaC 2024, Lecture Notes in Civil Engineering, vol 613. pp 351–359. https://doi.org/10.1007/978-3-031-73314-7_26
57. Blary F, Héricher A-MF (2021) L'ABBAYE CISTERCIENNE DE PREUILLY, UNE REDÉCOUVERTE. CReA-Patrimoine, 50, av. F.D. Roosevelt | CP 133/01, Brussels, Belgium 978-2-9602029-3-9
58. Cundari G, Milani G, Failla G, Nucera F, Santini A (2010) Two-step pushover analysis of an ancient masonry oil-mill in the Southern Italy. Science 133–134:361–366. https://doi.org/10.4028/www.scientific.net/AMR.133-134.361
59. Cundari GA (2022) La muratura. lineamenti generali. Master's thesis, Technical University of Milan, Milan, Italy
60. Sonon B, François B, Massart TJ (2012) A unified level set based methodology for fast generation of complex microstructural multi-phase rves. Comput Methods Appl Mech Eng 223–224:103–122. https://doi.org/10.1016/j.cma.2012.02.018
61. Beucher S (2011) Geodesic reconstruction, saddle zones & hierarchical segmentation. Image Anal Stereol 20:137–141. https://doi.org/10.5566/ias.v20.p137-141
62. Ehab Moustafa Kamel K, Massart TJ (2025) Towards automated image-based cohesive zone modeling of cracking in irregular masonry. Math Mech Solids 30(1):116–136. https://doi.org/10.1177/10812865241228825
63. Osher S, Sethian JA (1988) Fronts propagating with curvature-dependent speed: algorithms based on Hamilton-jacobi formulations. J Comput Phys 79(1):12–49. https://doi.org/10.1016/0021-9991(88)90002-2
64. Ghazi A, Berke P, Ehab Moustafa Kamel K, Sonon B, Tiago C, Massart TJ (2019) Multiscale computational modelling of closed cell metallic foams with detailed microstructural morphological control. Int J Eng Sci 143:92–114. https://doi.org/10.1016/j.ijengsci.2019.06.012
65. Ghazi A, Tiago C, Sonon B, Berke P, Massart TJ (2020) Computed tomography based modelling of the behaviour of closed cell metallic foams using a shell approximation. Mater Des 194:108866. https://doi.org/10.1016/j.matdes.2020.108866
66. Sonon B, Massart TJ (2013) A level-set based representative volume element generator and xfem simulations for textile and 3d-reinforced composites. Materials 6:5568–5592. https://doi.org/10.3390/ma6125568
67. Li A, Ehab Moustafa Kamel K, Wintiba B, Remmers J, Geers M, Massart TJ (2023) A level set-based procedure for the cohesive modeling of yarn-yarn contacts in woven composite rves. Compos Struct 304:116356. https://doi.org/10.1016/j.compstruct.2022.116356
68. Lee DT (1982) Medial axis transformation of a planar shape. IEEE Trans Pattern Anal Mach Intell PAMI 4(4):363–369. https://doi.org/10.1109/TPAMI.1982.4767267
69. Andersen ED (1995) Finding all linearly dependent rows in large-scale linear programming. Optim Methods Softw 6(3):219–227. https://doi.org/10.1080/10556789508805634